Research in Astronomy and Astrophysics, 25:105002 (11pp), 2025 October
© 2025. National Astronomical Observatories, CAS and IOP Publishing Ltd. All rights, including for text and data mining, AI training, and similar technologies, are reserved. Printed in China.
https://doi.org/10.1088/1674-4527/adf277
CSTR: 32081.14.RAA.adf277

Research on the Full-path Active Adjustment Strategy of Dual Reflector Antennas

Bin-Bin Xiang[1], Tian-Xiang Zheng[1], Shi-Ke Mo[1], Han-Wei Cui[1], Wei Wang[2], Shang-Min Lin[3], and Xue-Tong Yang[1]
[1] School of Mechanical Engineering, Xinjiang University, Urumqi 830017, China; xiangbinbin031@163.com
[2] School of Mechano-Electronic Engineering, Xidian University, Xi'an 710017, China
[3] Xi'an Institute of Optics and Precision Mechanics, Chinese Academy of Sciences, Xi'an 710119, China
Received 2025 June 10; revised 2025 July 13; accepted 2025 July 18; published 2025 August 15

Abstract

Active adjustment technology is used to solve the problem of reduced electrical performance of large reflector antennas caused by environmental factors. This technology is crucial for the operation of antennas under high-frequency working conditions. This paper proposes a full-path active adjustment strategy for dual-reflector antennas. This strategy takes into account the working mode of the adjustment mechanism under comprehensive influencing factors and achieves the optimal receiving performance at the full elevation by changing different adjustment algorithms. First, the relationship between the displacement of reflector and the wavefront phase was established based on geometric optics. Second, three adjustment algorithms of the double reflector antenna were compared and analyzed: based on the standard, the fit and the optimal parabolic surface, the calculation process of the adjustment amount was derived. An adjustment strategy model for multiple working conditions was proposed by introducing the elevation and the complexity coefficient and combining three adjustment algorithms. Finally, a finite element analysis was conducted on the dual-reflector antenna with a diameter of 110 m, and the advantages and disadvantages of different adjustment algorithms were compared. The results show that strategy model not only achieves the optimal state of the antenna at the full elevation, but also shortens the adjustment amount of the adjustment mechanism and improves the working efficiency of the antenna under various working conditions.

Key words: methods: analytical – techniques: radar astronomy – telescopes

1. Introduction

Radio telescope is a device that uses reflector antenna for receiving and transmitting radio waves. It has the advantages of high efficiency, low cost and unit weight of the large aperture part and broadband capability, as shown in Figure 1. As the aperture of the antenna increases, it will bring higher sensitivity and resolution. The sensitivity is related to the effective receiving area of the antenna. The larger the effective receiving area, the higher the aperture efficiency (Baars & Kärcher 2018; Baars 2020). When the aperture of the antenna exceeds 100 m, its huge structure is more susceptible to the influence of environmental load factors, thereby intensifying the increase of errors. This will increase the requirements for the active adjustment system of large-aperture antennas (Du et al. 2016).

The adjustment performance of the radio telescope depends on the wave front phase of the electromagnetic wave after it propagates through antenna systems such as the feed source, primary reflector and subreflector (Samii & Haupt 2015). Many scholars have conducted a large amount of research in order to improve the accuracy loss of the reflector. Ahn & Kihm (2020) improved the low-order aberration correction ability of deformed surfaces in applications by introducing coupling coefficients and modeling and optimizing the distribution of actuators based on the influence function. Based on the electromechanical coupling theory and finite element simulation, Wang et al. (2017, 2018) proposed a matrix multiplication algorithm for the adjustment of active reflector surfaces, which effectively improved the antenna gain and pointing accuracy. Maddalena & Prestage (2017) improved the pointing accuracy, surface accuracy and weather adaptability of the Green Bank Telescope based on the existing hardware and servo new instruments. Its high-frequency observation performance was enhanced (White et al. 2022). Lian et al. (2019) proposed two automatic adjustment strategies for a reflector based on laser measurement technology: one adjusts the reflector to the ideal position, and the other adjusts it to the optimal fitting position. Further, based on the approximate relationship between the elastic deformation of the panel and the adjustment value of the actuator, a panel adjustment matrix was proposed, which significantly improved the adjustment accuracy compared with the traditional model (Lian et al. 2021). Ban et al. (2024) proposed a neural network model combining multi-scale convolution and autonomous reemphasis layers based on convolutional neural networks, and applied it to the prediction of active adjustment of the primary reflector, achieving high-precision mapping between the node positions of the panel and the actuator adjustment amount. Sun et al. (2021) proposed an

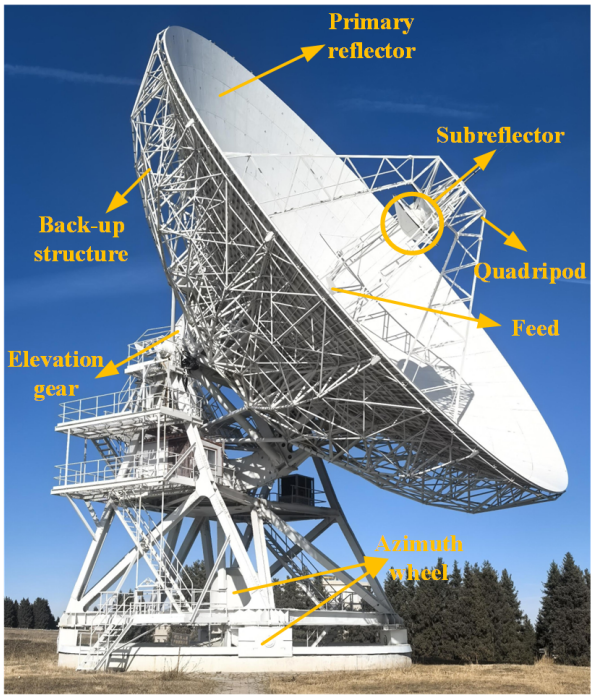


Figure 1. The Radio Telescope.

adjustment algorithm with constraints by using microwave holographic measurement technology and the panel plane fitting method. In order to improve the observation efficiency of the 65 m radio telescope in the *Ku* band and compensate for the influence of gravitational deformation, Chen et al. (2015) established a subreflector displacement compensation model based on the Stewart parallel mechanism and dynamic adjustment technology.

For the research contents of the above-mentioned scholars, multiple methods were adopted to compensate for the errors. However, most compensation algorithms are aimed at a single working state and do not consider the influence of working conditions on the compensation model under the errors of different working states of the antenna. In this paper, a full-path active adjustment strategy for the full elevation is proposed. By comparing the advantages and disadvantages of different adjustment algorithms, taking the wave front optical path difference as the discrimination criterion, and based on the current elevation and error scale, the performance of different adjustment mechanisms is effectively evaluated. The results show that the high precise compensation and an overall improvement in efficiency can be achieved by this strategy.

2. Analysis of the Influence of Full-path Errors

For large dual-reflector antenna systems, the huge structure further intensifies the influence of loads such as gravity and temperature, as well as manufacturing and installation errors. Figure 2 shows the load errors and the adjustment process. Among them, the gravitational load will cause deformation of the primary reflector and the subreflector, affecting the reflection path of the electromagnetic wave. The temperature change caused by thermal radiation leads to the thermal expansion or contraction of materials, resulting in changes in the geometric shape of the reflector. Antenna deformations caused by different load sources can be reflected in the wave front plane, thereby causing a reduction in the gain of the far-field pattern (Xiang et al. 2019).

2.1. Deformation of the Primary Reflector

The arrival of radio waves from infinity to the near field of the antenna can be equivalent to the form of plane waves. Under ideal conditions, the incident wave of the antenna can be reflected by the primary reflector and converge at the focus, and then reflected to the feed chamber through the subreflector.

Its ideal surface can enable the antenna to receive the maximum energy, as shown in Figure 3, where F is the focal point of the principal reflection surface, f is the focal length, C is a random node, r is the radius of this point relative to the center of the circle, and θ is the field angle of this point.

Based on the theory of geometric optics, the radio wave that originally passed through point C will move to point A due to the deformation of the panel. During the entire reflection process, the radio wave will travel a certain distance more or less, and this distance is called the optical path difference (OPD). In actual operation, the half-optical path difference is usually regarded as an indicator of the focusing performance of the primary reflector. According to the geometric relationship in Figure 3, the relationship between the half-optical path difference and the normal error or axial error can be obtained as:

$$\frac{\varepsilon_m}{2} = \varepsilon_1 \cos^2\frac{\theta}{2} = \varepsilon_n \cos\frac{\theta}{2} = \frac{\varepsilon_n}{\sqrt{1+\left(\frac{r}{2f}\right)^2}} \tag{1}$$

$$\xi_m = \frac{2\pi}{\lambda}\varepsilon_m \tag{2}$$

where λ is the wavelength, ξ_m is the phase error caused by the deformation of the primary reflector, ε_m is OPD. θ, ε_1, and ε_n are shown in Figure 3.

2.2. Offset of the Subreflector and the Feed Source

According to geometric optics, the relationship between the feed source and the subreflector can be equivalent to that between the primary reflector and the subreflector. Therefore, the method for calculating the optical path difference for the feed source is consistent with the subreflector offset. The rigid body displacement of the subreflector can be expressed in three-dimensional space by six degrees of freedom, namely the translation and rotation along the x, y, and z directions, which can be called the pose offset. Since the surface shape of the subreflector is a rotationally symmetric structure, the rotation

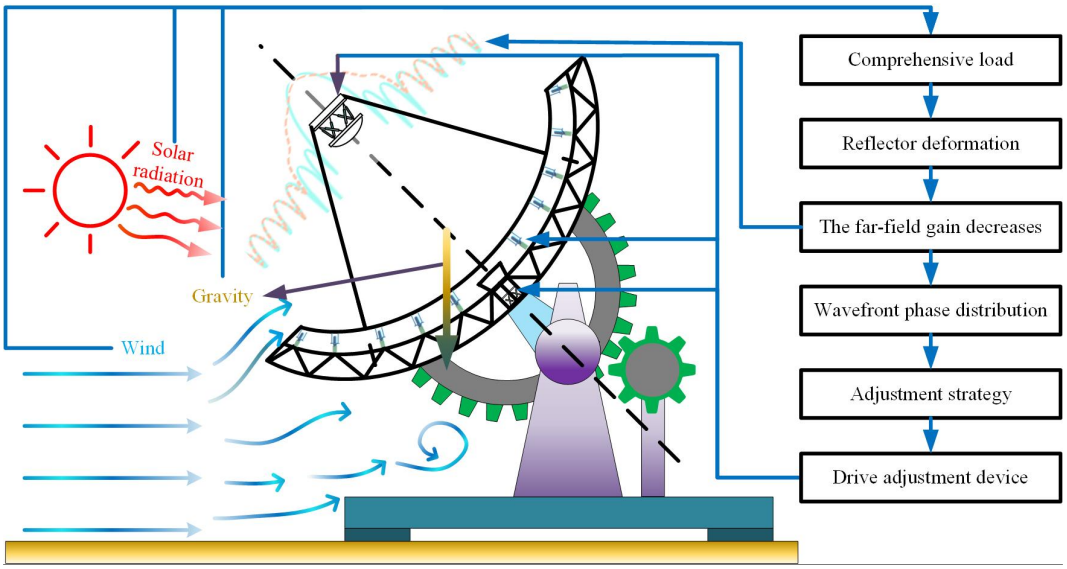


Figure 2. Environmental errors and active adjustment processes.

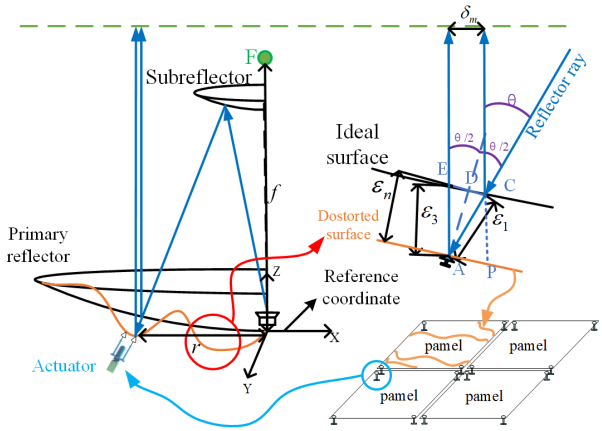


Figure 3. The primary reflector distortion causes the optical path difference.

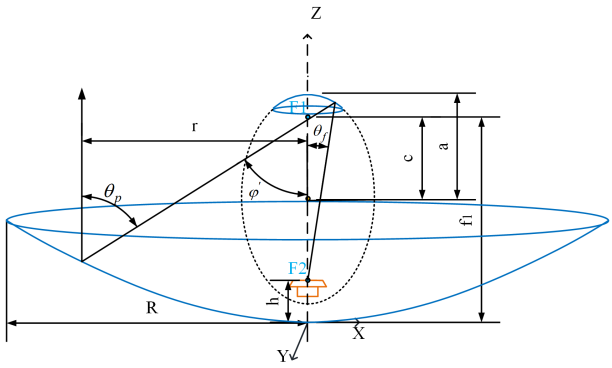


Figure 4. Gregory antenna geometric parameters.

around the z-axis causes no change in the wave front phase and does not need to be considered. Therefore, the five degrees are $p = [\Delta x_s, \Delta y_s, \Delta z_s, \Delta\varphi_x, \Delta\varphi_y]^{\mathrm{T}}$.

The OPD of the aperture caused by the translation and rotation of the subreflector and the feed source position of the Gregory antenna can be expressed as the superposition of the optical path difference changes caused by the deviations of different degrees of freedom, which can be expressed as:

$$\begin{aligned}
\varepsilon_{\mathrm{stx}} &= -\Delta x_t \cos\phi'(\sin\theta_p + \sin\theta_f) \\
\varepsilon_{sty} &= -\Delta y_t \sin\phi'(\sin\theta_p + \sin\theta_f) \\
\varepsilon_{stz} &= \Delta z_t(\cos\theta_p + \cos\theta_f) \\
\varepsilon_{st\varphi x} &= \Delta\varphi_{xt} \sin\phi'(c - a)(\sin\theta_p + M \cdot \sin\theta_f) \\
\varepsilon_{st\varphi y} &= \Delta\varphi_{yt} \cos\phi'(c - a)(\sin\theta_p + M \cdot \sin\theta_f) \qquad (3)
\end{aligned}$$

$$\varepsilon_{st} = \varepsilon_{stx} + \varepsilon_{sty} + \varepsilon_{stz} + \varepsilon_{st\varphi x} + \varepsilon_{st\varphi y} = C_s \cdot p \qquad (4)$$

where C_s is the geometric parameter matrix of the parabolic antenna, p is the deviation vector of the subreflector, M is the magnification of the double reflector surface, and Δx_t is the superposition of the displacements of the subreflector and the feed source along the x-direction, ε_{st} is the OPD caused by the offset of the subreflector. The remaining parameters are shown in Figure 4.

2.3. Comprehensive Wave Front Phase

The errors will change the propagation path of electromagnetic waves, causing the wave front phase to deviate from the ideal situation. Therefore, the wave front phase distribution can reflect the electromagnetic performance of the antenna. The full-path phase error can be expressed as:

$$\begin{aligned}
\xi_{\mathrm{all}} &= \sum_{i}^{N} \xi_i(\Delta t_i) \\
\Delta t_i &= (\Delta x_i, \Delta y_i, \Delta z_i, \Delta\varphi_{xi}, \Delta\varphi_{yi}) \qquad (5)
\end{aligned}$$

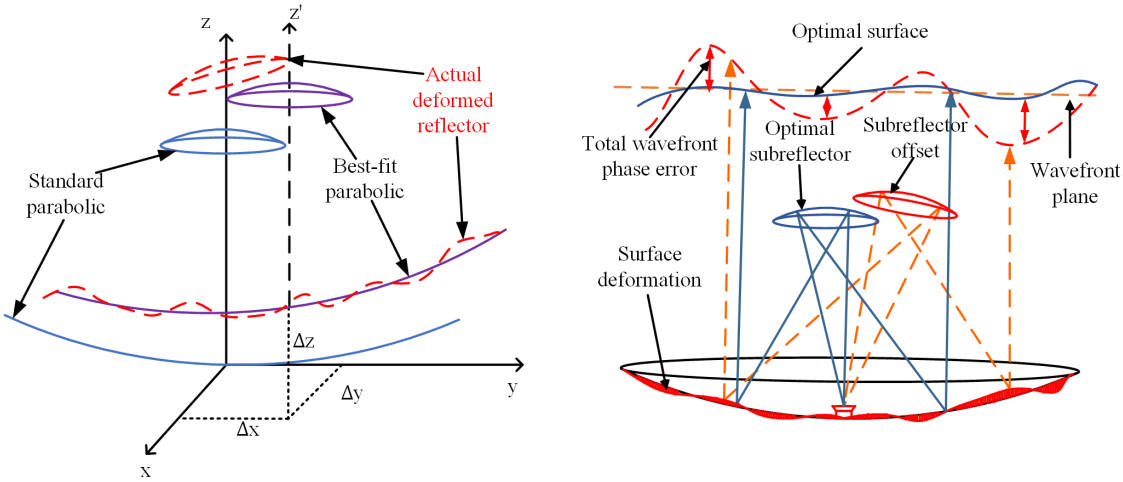


Figure 5. Schematic diagram of the adjustment process of BFP, SP(a) and OSF(b).

where ξ_{all} is the total phase error, ξ_i is the phase error caused by the ith mechanism, and Δt_i is the offset of the ith component. The full-path adjustment mechanism compensates for the wave front phase error by adjusting each degree of freedom of the antenna (such as pitch, azimuth, subreflector position, etc.). If the adjustment amount of each mechanism is Δa_i, then the wave front phase after adjustment can be expressed as:

$$\xi' = \xi_{\text{all}} + \sum_{i=1}^{n} \frac{\partial \xi_{\text{all}}}{\partial \Delta a_i} \Delta a_i \tag{6}$$

where ξ' is the residual wave front phase after adjustment, $\frac{\partial \xi_{\text{all}}}{\partial \Delta a_i}$ indicates the influence characteristics of the ith adjustment mechanism on the total phase, and n is the number of adjustment mechanisms.

3. Establish the Adjustment Strategy Model

At present, the active adjustment methods used for dual-reflector antennas are respectively based on the standard parabolic (SP), the best-fit parabolic (BFP) and the optimal surface (OSF) of the minimum wave front residual. Different adjustment processes are shown in Figure 5. This paper will combine the characteristics of different adjustment methods to study the full-path adjustment strategy in order to achieve the overall compensation of the error of the dual-reflector antenna.

3.1. Best-fit Parabolic Model

BFP seeks the fitting surface with the minimum geometric residual on the deformed primary reflector. This method can compensate for the deformation error of the reflector as much as possible. Afterwards, the propagation path is optimized by moving the subreflector to the focal point of the fitting surface, as shown in Figure 5. By obtaining the parameters of the mating surface, the adjustment amount of the subreflector can be further calculated. Its fitting parabolic equation can be expressed as:

$$F(x, y) = \frac{(x + \Delta x_f)^2 + (y + \Delta y_f)^2}{4(f_1 + \Delta f_f)} + \Delta z_f. \tag{7}$$

The fitting parameters of the parabolic equation are solved by using the least square method based on the discrete point deformation, and the vector can be expressed as $c = [\Delta x_f, \Delta y_f, \Delta z_f, \Delta f_f]$. Through the parameter vector, we can obtain the new parabolic equation, which is used to solve the adjustment amount of the subreflector. Since the new focus of the fitting equation has a certain offset relative to the standard parabolic and the position of the feed source hardly changes during the antenna operation, it can be considered that the feed source is always at the vertex of the standard parabolic. The adjustment amount of the subreflector is calculated by combining the spatial position of the focus and the vertex of the subreflector. It can be expressed as:

$$\begin{cases} \Delta a_{sfx} &= \Delta x_f \left(1 + \frac{a-c}{f_1 + \Delta f}\right) + \Delta x \\ \Delta a_{sfy} &= \Delta y_f \left(1 + \frac{a-c}{f_1 + \Delta f}\right) + \Delta y \\ \Delta a_{sfz} &= \Delta z_f + \Delta f + \Delta z \\ \Delta \varphi'_{sfx} &= \tan\left(\frac{\Delta y_f}{h + c + a + \Delta z_f}\right) + \Delta \varphi_x \\ \Delta \varphi'_{sfy} &= \tan\left(\frac{\Delta x_f}{h + c + a + \Delta z_f}\right) + \Delta \varphi_y \end{cases} \tag{8}$$

where each calculation parameter is shown in Figure 4.

3.2. Standard Parabolic Model

Suppose that the OPD caused by the overall deviation in the dual-reflector antenna system is ε_{all}. The OPD caused by the offset of the subreflector is ε_s. Then the residual OPD adjusted based on the standard parabolic can be expressed as:

$$\varepsilon_{\text{std}} = \varepsilon_{\text{all}} + \varepsilon_s. \tag{9}$$

For standard parabolic, the rigid body displacement is the opposite of the subreflector offset. However, the rotation cannot be based on the vertex of the principal parabolic surface. It is necessary to use a gyroscope or other devices to measure the angle of the subreflector in the global coordinate system in real time. The actual rotation can be expressed as the value of the elevation deviation and the feed source angle deviation. Therefore, the vertex of the subreflector can be coincident with the focus of the primary reflector, and then its rotation amount can be adjusted to coincide with the position of the standard subreflector. The specific value is expressed as:

$$\begin{aligned} \Delta a_{ssx},\ \Delta a_{ssy},\ \Delta a_{ssz} &= -\Delta x_s,\ -\Delta y_s,\ -\Delta z_s \\ \Delta a_{ss\varphi x} &= -\theta \end{aligned} \tag{10}$$

where Δa_{ssx} is the adjustment amount of the subreflector along the x-axis.

3.3. Optimal Surface Model

The optimal surface is an adjustment method aimed at minimizing the total OPD. The same OPD distribution is caused by the offset and the pose adjustment of the subreflector, the OPD can be further deduced after adjustment of the subreflector, and it can be expressed as:

$$\varepsilon_{\text{opt}} = \varepsilon_{\text{all}} + C_s \cdot \Delta a_s. \tag{11}$$

Based on discrete points, the adjustment amounts of all degrees of freedom can be approximately obtained by the least square method to improve the efficiency of adjustment solution. The adjustment vector can be expressed as:

$$\Delta a_{\text{sopt}} = -(C_s^T C_s)^{-1}(C_s^T \varepsilon_{\text{all}}) \tag{12}$$

where C_s is the geometric parameter matrix of the parabolic antenna, Δa_{sopt} is the adjustment amount of each degree of freedom of the subreflector.

Through the above derivation, we respectively obtained the adjustment equations required by the three adjustment algorithms. The calculation process for the adjustment of the primary reflector is obtained based on the OPD distribution after the adjustment of the subreflector, and the calculation process is consistent. This method can be referred to (Zheng et al. 2024), and will not be described here. Then, these methods are applied to the super-large antenna system with full elevation to establish the optimal adjustment strategy.

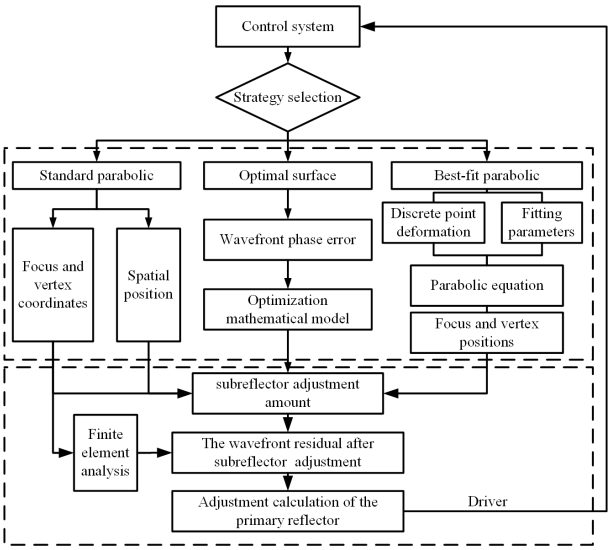


Figure 6. An active adjustment process based on strategies.

3.4. Comprehensive Adjustment Strategy Model

For a dual-reflector antenna with a primary reflector and subreflector system, each adjustment method will change the distribution of the wave front phase to varying degrees. To conduct a unified analysis, we divide the comprehensive error into large-scale errors (centimeter level) and small-scale errors (millimeter level). Large-scale errors are manifested as the overall offset and pose change of the antenna, with a relatively wide influence range. Small-scale errors are manifested as local deviations such as installation and surface deformation. The superposition of the two is the overall wave front error.

The rigid body displacement of the subreflector (translation and rotation) will cause changes in the overall optical path difference. Therefore, large-scale errors can be corrected quickly and effectively through the adjustment of the subreflector, while small-scale errors are usually difficult to be compensated through the subreflector. Due to the limitations of accuracy and displacement length, the actuator is more suitable for compensating small-scale errors by adjusting the independent panel. By combining the use of the main and secondary reflector adjustment systems, compensation can be made respectively for errors of different scales. Thereby we achieve the optimization of the overall performance of the antenna. The specific process is shown in Figure 6.

The specific process of adjusting the strategy is as follows:

1. The position and deformation of the reflector are measured by laser measurement or angle sensor, and the wave front optical path is further derived.
2. Based on the measured wave front phase and elevation position, select the appropriate full-path adjustment algorithm.

3. According to different adjustment algorithms, the corresponding calculation parameters are obtained, such as the spatial coordinates and deformation amounts of each discrete point on the reflector used for the adjustment of the BFP.
4. Obtain the subreflector adjustment amount and calculate the adjusted wave front phase.
5. The adjustment amounts of actuators are further calculated based on the primary reflector calculation method.
6. Adjust the subreflector and the actuator simultaneously for adjustment through the control system.

To clearly distinguish the performance of the three adjustment algorithms, we introduce the elevation value and the comprehensive influence coefficient. The wave front phase after the transformation of a point on the principal parabolic can be written as:

$$\xi_m = \frac{2\pi}{\lambda} \cdot \mathrm{OPD}(\delta_z)$$
$$\delta_z = \delta_{z\,g}(\theta, \mu) \cdot \frac{r^2}{R^2} \tag{13}$$

where $\delta_{zg}(\theta)$ is the axial displacement under the gravity. When the elevation θ decreases, its displacement at the full elevation can be approximately expressed as $\delta_{z\,g}(\theta) \approx \delta_{z\,\max}\cos\theta + \mu\delta_{\mathrm{other}}$. The value of μ is between 0 and 1, $\delta_{\mathrm{other}}s$ is the error term caused by environmental factors other than gravity. Compared with the total displacement, its proportion is relatively small. When in a windless and moderately warm environment, $\mu = 0$. When θ approaches 0, the axial displacement reaches its maximum value, thereby causing the wave front phase error to reach its maximum value. Moreover, the distribution of the phase error is proportional to r^2, and the distortion in the edge region is more severe. We perform polynomial decomposition on the deformation amount:

$$\delta_z(r, \theta, \mu) = a_0(\theta, \mu) + a_1(\theta, \mu)r + a_2(\theta, \mu)r^2 + \cdots. \tag{14}$$

According to the equation of the best fit parabolic, its translation amount will compensate for the constant term $a_0(\theta, \mu)$, and the adjustment of the focal length will compensate for the secondary term $a_2(\theta, \mu)r^2$ and a small part of the tertiary term. Therefore, the residual adjusted using the BFP can be expressed as:

$$\delta'_z(r, \theta, \mu) = a_1(\theta, \mu)r + \left(a_2(\theta, \mu) - \frac{\Delta F}{4F^2}\right)r^2 + a_3(\theta, \mu)r^3 + \cdots. \tag{15}$$

When the elevation is low or the influence of environmental factors is significant, $\cos\theta$ and μ will increase, resulting in a significant increase in the high-order term. Assuming that gravity is the main deformation factor, the compensated residual wave front phase can be written as:

$$\xi(r, \theta) = \frac{2\pi k}{\lambda}\cos\theta \cdot \frac{r}{R}\left(1 + \frac{r}{R} + \beta\frac{r^3}{R^3}\right) \tag{16}$$

where k is the deformation coefficient, and β is the higher-order term scale factor, whose value is much less than 1. The influence of the quadratic term phase error can be alleviated by optimizing the focal length. However, as the elevation increases, the high-order aberrations (fourth term and above) are significantly enhanced. It is impossible to effectively compensate by merely BFP, and the wave front phase needs to be directly optimized through the adjustment of the subreflector.

Based on the above error decomposition and derivation, it can be concluded that at a low elevation, the structure of the antenna undergoes significant rigid body displacement or low-order deformation due to the effect of gravity. The wave front error caused by deformation is usually the low-order term. Adjusting the five degrees of freedom of the subreflector can specifically compensate for the low-order terms and also compensate for a certain amount of high-order terms.

The OSF aims to minimize the wave front phase error and comprehensively considers the errors of the primary reflector, the subreflector and the feed source. Although this method can achieve the optimal compensation under the full path, the OPD distribution caused by the adjustment of different degrees of freedom is always constant and has a certain deviation from the ideal parabolic surface. At high elevation, due to the small deformation of the primary reflector and the single source of error, the fitting parameters of the BFP for the quadratic term are relatively accurate, thus it can better fit the parabolic form of the primary reflector.

According to the size of the wave front error distribution scale, we can obtain the corresponding adjustment strategy as follows: when the elevation is low, the OSF is used for adjustment; when the elevation is high, the BFP is used for adjustment. Further, by combining the adjustment methods of the primary reflector, the adjustment amount under the full-path is obtained as:

$$\begin{cases} \theta > \rho: \begin{cases} \Delta a_s = [\Delta a_x, \Delta a_y, \Delta a_z, \Delta\varphi'_x, \Delta\varphi'_y] \\ u_{\mathrm{fit}} = (F^T T^T T F)^{-1} F^T T^T T A p^T \end{cases} \\ \theta < \rho: \begin{cases} \Delta a_{\mathrm{opt}} = (C_s^T C_s)^{-1}(C_s^T \varepsilon_{\mathrm{all}}) \\ u_{\mathrm{opt}} = (M^T M)^{-1} M^T(\varepsilon_{\mathrm{all}} + C_s \Delta a_{\mathrm{opt}}) \end{cases} \end{cases} \tag{17}$$

where $M = TF$, F is the surface shape influence matrix, and T is the OPD conversion matrix, ρ is the elevation, θ is the determination value, $\varepsilon_{\mathrm{all}}$ is the wave front OPD before adjustment, Δa_s is the subreflector adjustment amount based on the BFP, Δa_{opt} is the subreflector adjustment amount based on OSF, A is the geometric relationship of the deformation points within the parabolic, p is the parameter vector for fitting the parabolic equation.

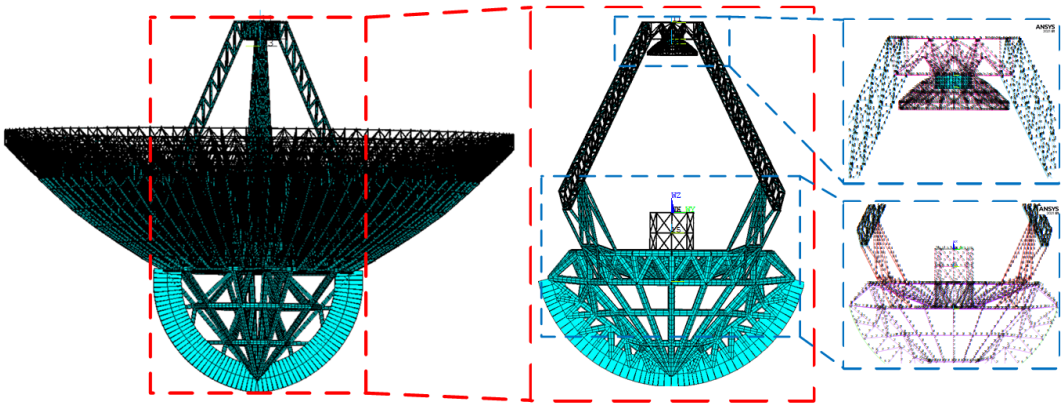


Figure 7. Finite element model of the reflector of the 110 m double reflector.

4. Simulation Verification

First, a dual-reflector antenna with an aperture of 110 m was established as shown in Figure 7. Then, gravitational loads in different directions were applied to the model, and the deformation of the primary reflector and the offset of the subreflector were obtained within the elevation range of 10°–90°.

Based on the principle of linear superposition, the total OPD caused by the deformation of the subreflector and the primary reflector was obtained as shown in Figure 8. The RMSE of optical path differences were 42.32 mm and 86.79 mm at 70° and 30° respectively. According to the distribution trend, it can be obtained that as the antenna elevation decreases, the main influencing factor is the offset in the y direction of the subreflector, while the influences in the x and z directions are relatively small. The trend is consistent with the description of the comprehensive error in this paper.

Then, the adjusted optical path difference distribution is obtained by using the different adjustment methods described in this paper. It needs to be emphasized that most of the errors of large antennas during operation are mainly caused by gravity. Therefore, only the deformation of the antenna under gravitational load is simulated in this paper.

4.1. Accuracy Analysis of Collaborative Adjustment

To reduce the total optical path difference, we respectively adopt different adjustment methods for compensation calculation, as shown in Figures 9–14. The results show that when the elevation is 70°, the RMSE of OPD adjusted by BFP is the smallest. When the elevation is 30°, the OPD after adjustment using OSF is relatively lower. Table 1 lists the rms of optical path differences under different elevations. In contrast, the OPD within the full elevation range using the SP adjustment method is relatively large. The pointing offset was obtained by analyzing the far-field pattern, which reflects the degree of deviation between the actual pointing direction of the antenna and the theoretical target direction. In addition, the Zernike

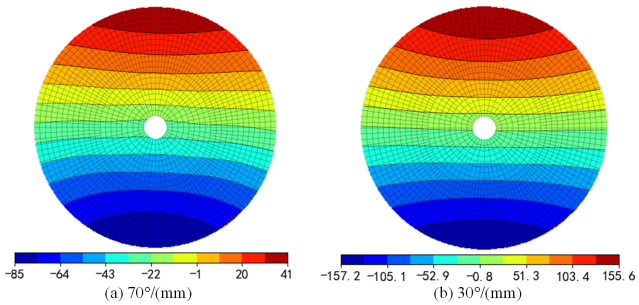


Figure 8. The distribution of the total OPD at elevation 70° and 30°.

polynomial was used to fit the OPD, and the influence of the overall compensation on the pointing deviation was evaluated using Tilt and Coma as shown in Table 2. It can be obtained that the coefficients fitted by the three methods have been significantly reduced, and the values are similar, indicating that the adjustment effects of the three methods on the pointing offset are similar. Moreover, the pointing offset after adjusting the subreflector with the OSF maintains good performance at the full elevation at 24 GHz.

To obtain an overall comparison, we analyzed the RMSE of OPD adjusted from 10° to 90°. Figure 15 shows the RMSE after the subreflector adjustment, and Figure 16 shows the RMSE after the primary reflector adjustment. It can be known from the results that the error after adjustment using the SP is relatively large. The adjusted total elevation error distribution is consistent with the above. Furthermore, it can be concluded that the effect of the subreflector adjustment will affect the final result. The change in the intersection point position is due to the proximity of the error values, the OPD distribution after adjusting the subreflector using OSF is more uniform.

4.2. Comparison of Adjustment Amounts

Different adjustment methods require different strokes for the adjustment mechanism. The greater the adjustment amount

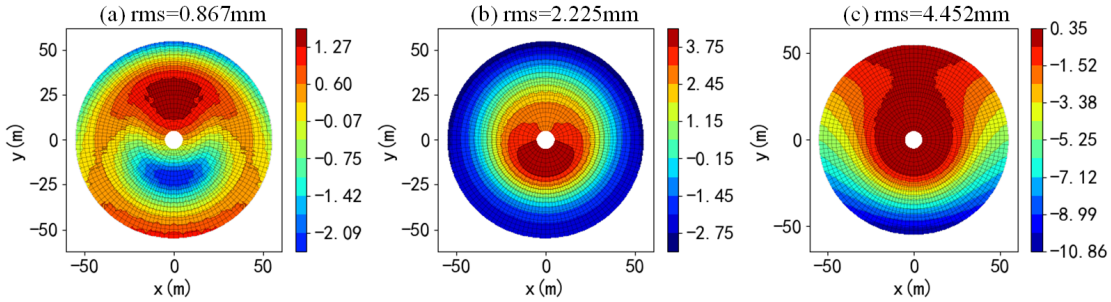


Figure 9. The OPD after subreflector adjustment using BFP(a), OSF(b) and SP(c) at 70°.

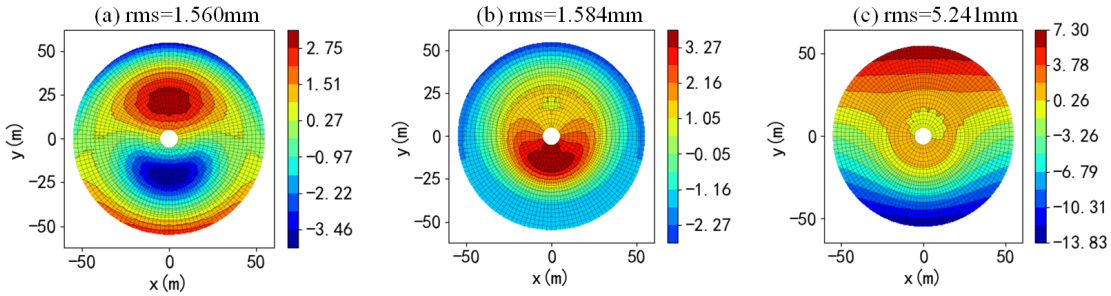


Figure 10. The OPD after subreflector adjustment using BFP(a), OSF(b) and SP(c) at 50°.

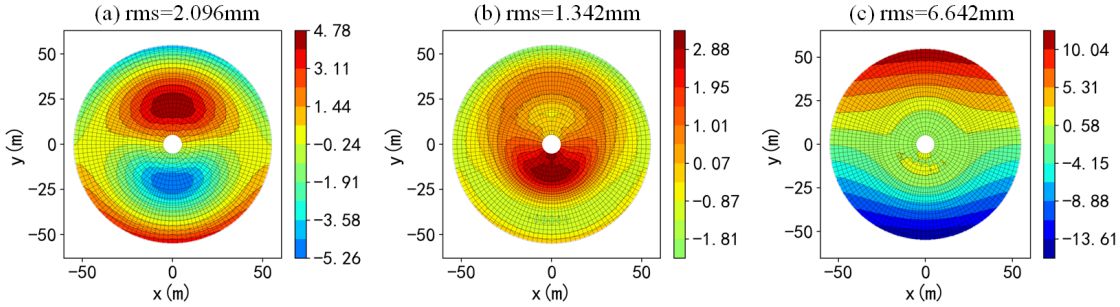


Figure 11. The OPD after subreflector adjustment using BFP(a), OSF(b) and SP(c) at 30°.

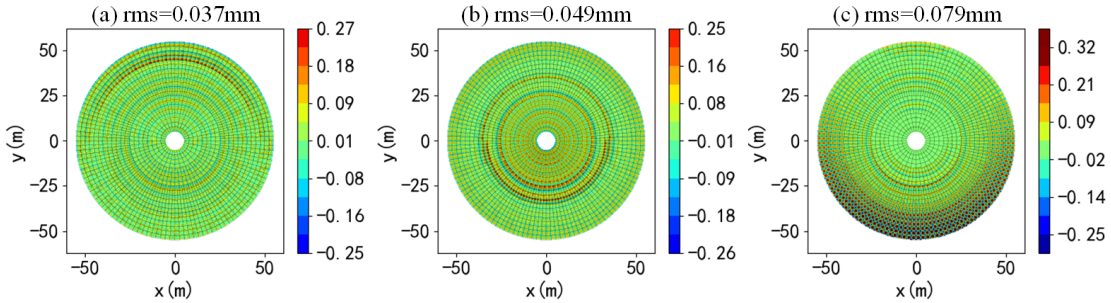


Figure 12. The OPD after adjustment using BFP(a), OSF(b) and SP(c) at 70°.

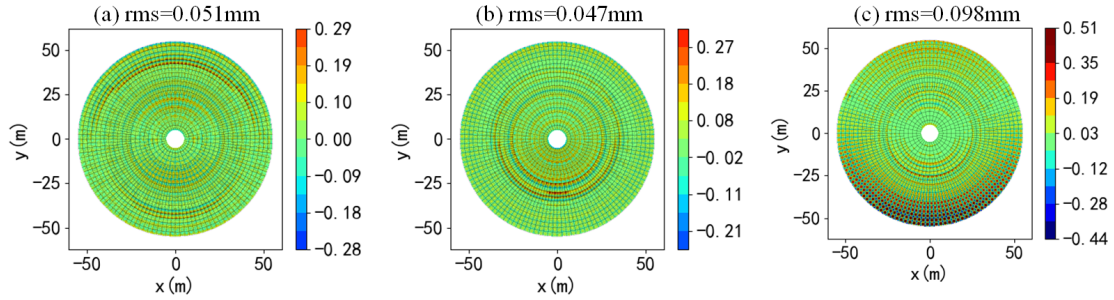


Figure 13. The OPD after adjustment using BFP(a), OSF(b) and SP(c) at 50°.

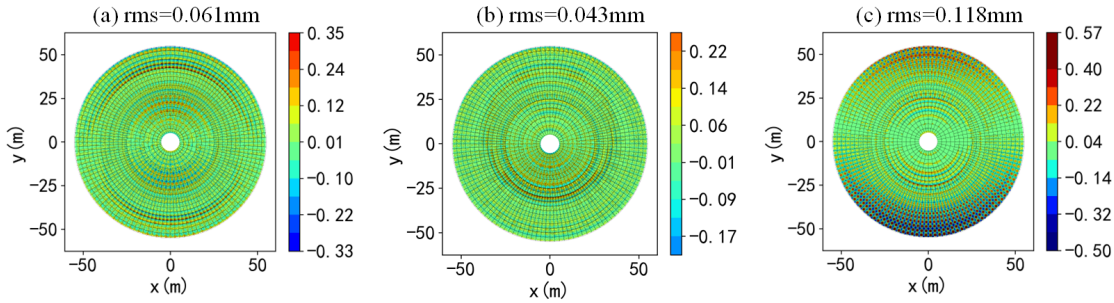


Figure 14. The OPD after adjustment using BFP(a), OSF(b) and SP(c) at 30°.

Table 1
The rms Values of Optical Path Differences at Different Elevation (I)

Case	A-B/mm	BFP/mm		OSF/mm		SP/mm	
		A-S	A-M	A-S	A-M	A-S	A-M
90°	32.61	0.285	0.029	2.352	0.049	3.916	0.071
70°	42.32	0.867	0.037	2.225	0.049	4.452	0.079
50°	65.92	1.567	0.051	1.865	0.047	5.585	0.098
30°	86.79	2.096	0.062	1.342	0.044	6.642	0.118
10°	99.30	2.379	0.069	0.841	0.043	7.250	0.129

Note. A-B represents the adjustment of before, A-S indicates that after the subreflector is adjusted, and A-M indicates that after the primary reflector is adjusted.

is, the more time will be spent and the corresponding system response speed will decrease, which will increase the requirement for real-time compensation. As shown in Figures 17 and 18, the displacement of the rigid body using the SP is bigger than other two methods and the adjustment angle is the smallest. Therefore, the adjustment speed should be higher. The adjustment displacement and rotation values of the OSF adjustment method are relatively balanced. The adjustment angle of the BFP is large, while the displacement is relatively small. So, it can be concluded that different adjustment methods have different performance requirements for the subreflector adjustment mechanism. For methods with a large amount of adjustment, the speed and accuracy of adjustment can be appropriately increased. For methods with larger rotation amounts, the collaborative ability of the adjustment mechanism can be prioritized for improvement.

Figure 19 shows the adjustment amounts of the primary reflector actuators for the three methods. At a low elevation, the adjustment amount of the OSF is relatively small. At a high elevation, the adjustment amount of the BFP is relatively small. Therefore, using adjustment strategies for compensation can not only improve the overall accuracy, but also effectively reduce the adjustment time.

5. Discussion

This paper proposes a full-path adjustment strategy for dual-reflector antennas. First, the wave front phase change caused by the deviation in the full path of the radio telescope was derived. Second, with the wave front phase as the optimization objective, the global adjustment strategy is obtained based on the error scale by combining the adjustment methods of the BFP and the OSF. According to the simulation results, when the elevation is low, the OSF is increased by up to 37.7% compared with the BFP and by up to 66.6% compared with the SP. When the elevation is high, the BFP is increased by up to 40.8% compared to the OSF and 59.1% compared to the SP. On the one hand, the adjustment strategy largely increases the accuracy and maintains a better state during operation. On the other hand, the response speed of each adjustment mechanism

Table 2
The rms Values of Optical Path Differences at Different Elevation (II)

Case	A-B			BFP			OSF			SP		
	P-O(arcsec)	Tilt	Coma	P-O(arcsec)	Tilt	Coma	P-O(arcsec)	Tilt	Coma	P-O(arcsec)	Tilt	Coma
90°	0.14	4.93e-5	9.95e-7	0.0	7.65e-7	1.15e-6	0.0	2.63e-7	3.97e-7	0.0	1.32e-6	1.94e-6
70°	4.81	1.45e-3	3.81e-6	0.082	1.24e-7	4.04e-7	0.011	1.30e-6	1.95e-6	0.205	2.49e-7	3.31e-7
50°	9.1	2.69e-3	4.36e-7	0.123	4.97e-7	4.02e-7	0.02	4.85e-7	7.74e-7	0.45	3.35e-7	5.47e-7
30°	12.3	3.61e-3	1.70e-6	0.24	5.09e-7	3.07e-7	0.035	6.39e-7	9.94e-7	0.69	6.66e-7	8.51e-7
10°	14.02	4.08e-3	2.23e-6	0.61	6.95e-7	5.25e-7	0.039	8.87e-7	1.51e-6	0.77	5.96e-7	7.33e-7

Note. A-B represents the adjustment of before. P-O is the pointing offset after the subreflector adjustment. The aberration coefficient is the fitting result after full-path adjustment.

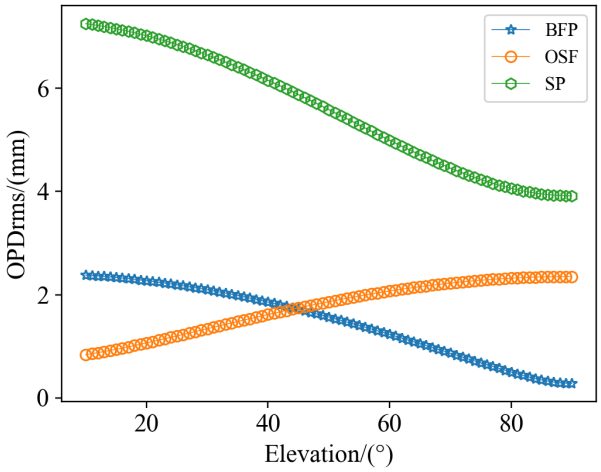


Figure 15. The OPD adjusted for the subreflector at full elevation.

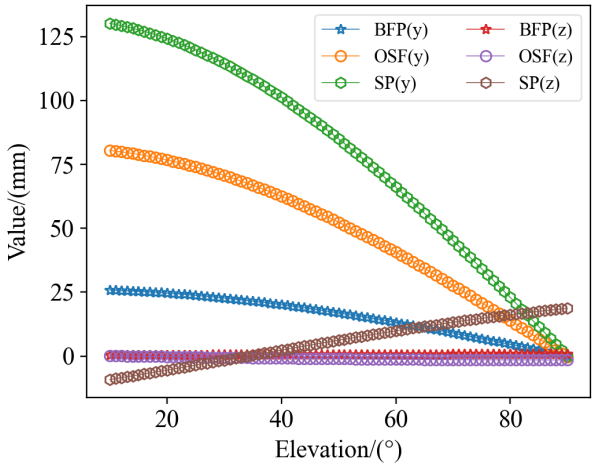


Figure 17. The subreflector adjustment along the translation of y and z.

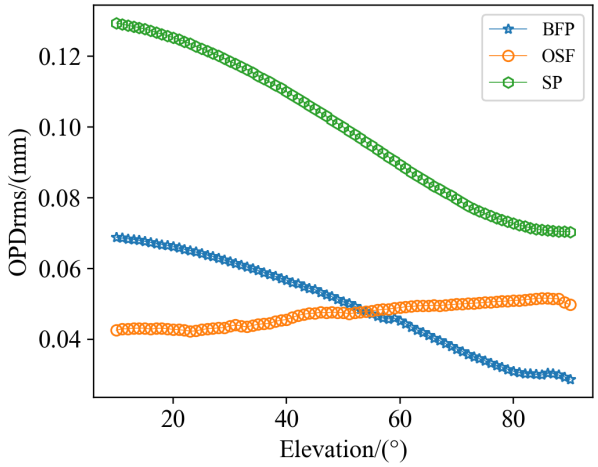


Figure 16. The OPD after full-path adjustment at full elevation.

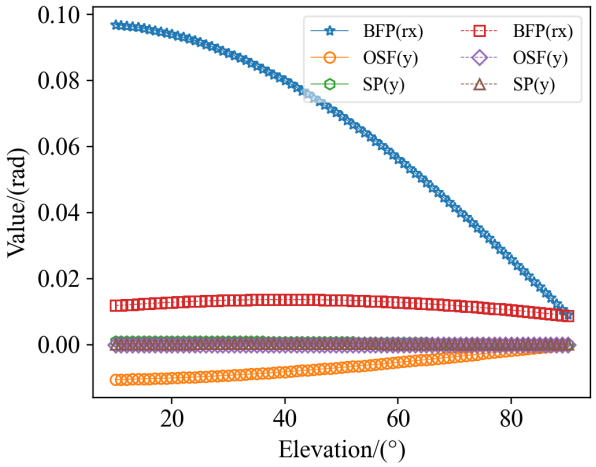


Figure 18. The subreflector adjustment along the rotation of x and y.

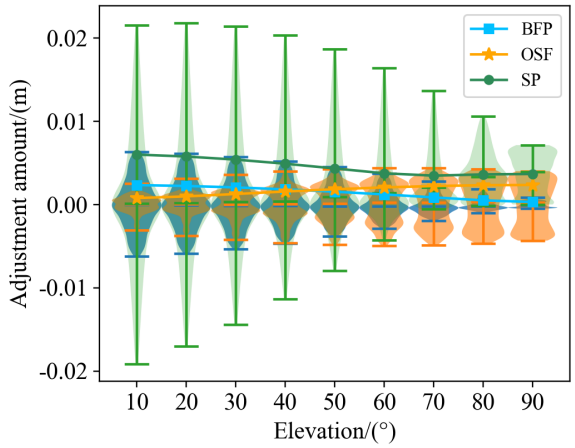


Figure 19. The adjustment amount of the actuator on the primary reflector.

has been enhanced. This strategy provides a theoretical basis for the intelligent real-time adjustment of large antennas.

Acknowledgments

This research was funded by the National Natural Science Foundation of China (Nos. 12363011, 52275270, 52275269), Natural Science Foundation of Xinjiang Uygur Autonomous Region (No. 2023D01C22), the Tianchi Talents Program of Xinjiang, the National Key Basic Research Program of China (No. 2021YFC2203501) and the Xinjiang Postdoctoral Foundation.

ORCID iDs

Bin-Bin Xiang https://orcid.org/0000-0001-7071-4779

References

Ahn, K., & Kihm, H. 2020, OptLE, 126, 105864
Baars, J. W. M. 2020, URSB, 2020, 10
Baars, J. W. M., & Kärcher, H. J. 2018, in Radio Telescope Reflectors: Historical Development of Design and Construction, ed. BURTON, BERTOLA, & CESARSKY (Berlin: Springer), 63
Ban, Y., Shi, S., Wang, N., et al. 2024, RAA, 24, 065024
Chen, L., Sun, Z. X., Wang, J. Q., et al. 2015, Prog. Electromagnetics Res. M., 44, 59
Du, B., Wu, Y., Zhang, Y.-F., et al. 2016, RaCT, 42, 1
Lian, P., Wang, C., Xue, S., et al. 2021, ITAP, 69, 6351
Lian, P., Wang, C., Xue, S., et al. 2019, IET Microwaves, Antennas & Propagation, 13, 2669
Maddalena, R. J., & Prestage, R. M. 2017, in 32nd URSI GASS, 19 *(Montreal, 19-26 August 2017)* ed. P. Wilkinson (Gent: URSI)
Samii, Y., & Haupt, R. 2015, IAPM, 57, 85
Sun, Z., Wang, J., Yu, L., et al. 2021, RAA, 21, 038
Wang, C., Li, H., Ying, K., et al. 2018, Int. J. Antennas and Propagation, 2018, 3903412
Wang, C., Xiao, L., Wang, W., et al. 2017, RAA, 17, 043
White, E., Ghigo, F. D., Prestage, R. M., et al. 2022, A&A, 659, A113
Xiang, B., Wang, C., & Lian, P. 2019, Int. J. Antennas and Propagation, 2019, 5062545
Zheng, T., Xiang, B., Cui, H., et al. 2024, RAA, 24, 075018